

**Stress Changes on the Garlock fault during and after the
2019 Ridgecrest Earthquake Sequence**

1. **Marlon D. Ramos**₁ ramosmd@umich.edu
2. **Jing Ci Neo**₁ neoj@umich.edu
3. **Prithvi Thakur**₁ prith@umich.edu
4. **Yihe Huang**₁ yiheh@umich.edu
5. **Shengji Wei**₂ shjwei@ntu.edu.sg

1. **University of Michigan, Department of Earth and Environmental Sciences**
2. **Nanyang Technological University of Singapore, Asian School of the Environment**

47 **Abstract**

48 The recent 2019 Ridgecrest earthquake sequence in Southern California jostled the
49 seismological community by revealing a complex and cascading foreshock series that culminated
50 in a M7.1 mainshock. But the central Garlock fault, despite being located immediately south of
51 this sequence, did not coseismically fail. Instead, the Garlock fault underwent post-seismic creep
52 and exhibited a sizeable earthquake swarm. The dynamic details of the rupture process during the
53 mainshock is largely unknown, as is the amount of stress needed to bring the Garlock fault to
54 failure. We present an integrated view of how stresses changed on the Garlock fault during and
55 after the mainshock using a combination of tools including kinematic slip inversion, Coulomb
56 stress change, and dynamic rupture modeling. We show that positive Coulomb stress changes
57 cannot easily explain observed aftershock patterns on the western section of the Garlock fault, but
58 are consistent with where creep was documented on the central Garlock fault section. Our dynamic
59 model is able to reproduce the main slip asperities and kinematically estimated rupture speeds (\leq
60 2 km/s) during the mainshock, and suggests the temporal changes in normal and shear stress on
61 the Garlock fault were greatest near the end of rupture. The largest static and dynamic stress
62 changes on the Garlock fault we observe from our dynamic model coincide with the creeping
63 region, suggesting that positive stress perturbations could have caused this during or after the
64 mainshock rupture. This analysis of near-field stress change evolution gives insight into how the
65 Ridgecrest sequence influenced the local stress field of the northernmost Eastern California Shear
66 Zone.

67 **Introduction**

68 The 2019 Ridgecrest earthquake sequence involved the rupture of a left-lateral M6.4
69 foreshock that occurred on July 4, and a right-lateral M7.1 mainshock that occurred on July 6 and
70 initiated approximately 13 km northwest of the foreshock epicenter (Fig. 1). This sequence was
71 characterized by the activation of multiple orthogonal fault segments that are collectively referred
72 to as the Little Lake fault zone (Llfz). Coseismic rupture of these faults continues to produce
73 aftershocks, but it did not influence the adjacent left-lateral Garlock fault to fail. Instead, this
74 sequence caused as much as three centimeters of surface creep on the Garlock fault that has been
75 detected geodetically (Barnhart et al., 2019; Ross et al., 2019).

76 Several kinematic slip models have been developed to estimate the evolution of slip and
77 rupture propagation during this highly complex sequence (Barnhart et al., 2019; Goldberg et al.,

78 2019; Liu et al., 2019; Ross et al., 2019). These models are consistent in the respect that a majority
79 of foreshock and mainshock slip is limited to the upper 10 km depth. Positive stress change
80 amplitudes (~ 0.5 MPa) are suggested from static Coulomb modeling and generally coincide with
81 the ~ 25 km long region of creep on the central Garlock fault segment (Barnhart et al., 2019). But
82 the dynamic details of rupture and how stresses were mediated by the seismic wavefield remains
83 hazy. The Garlock fault was apparently not near critical failure, or else we would have observed
84 coseismic rupture there as well; this implies that the stress perturbations were unable to bring shear
85 stresses to overcome the static Garlock fault strength.

86 When the Garlock fault will slip again is a major unknown. The Garlock fault extends for
87 ~ 260 km and is geometrically segmented into western, central, and eastern sections that are
88 characterized by variations in geologic slip-rate and recurrence interval (Davis and Burchfiel,
89 1973; Hill et al., 1953, McGill and Sieh, 1991; Fig. 1). Astiz and Allen (1983) analyzed historical
90 seismicity on this fault and hypothesized that a rupture on the eastern Garlock segment may be
91 more likely given its apparent seismic gap, though both the central and western sections can
92 independently support $\sim M7$ earthquakes. Paleoseismic evidence suggests historic, non-periodic
93 surface rupture for the central Garlock segment (Dawson et al., 2003), which is the closest segment
94 to the Ridgecrest sequence. Portions of this segment also experienced a swarm of low-magnitude
95 earthquakes ($ML < 3.2$; Ross et al., 2019) and underwent creep. How the strain accumulation
96 budget of the central Garlock fault was influenced by the recent Ridgecrest sequence is enigmatic
97 and warrants further scrutiny for seismic hazard analysis. A spatial separation between the
98 mainshock and Garlock fault planes is furthermore subject to uncertainty, as is the possibility of
99 rupture branching from a segment of the Garlock fault onto an adjacent segment or to the San
100 Andreas fault during a future earthquake. In particular, the central and western segments have co-
101 ruptured within the last 10 kya, despite a step-over structure in between them (Madugo et al.,
102 2012). Assessing the possibility of how close the Garlock fault is to failure depends on both the
103 static and dynamic stress perturbations from the Ridgecrest sequence.

104 We aim to present a physically consistent picture of the stress interaction vis-à-vis the
105 Garlock fault during and after the Ridgecrest sequence. We draw from updated kinematic
106 inversion results that utilizes teleseismic and near-field strong ground-motion recordings to
107 independently constrain the fault slip amplitude, extent and rupture initiation locations of the
108 foreshocks and M7.1 mainshock. This is then used to inform our static Coulomb stress analysis

109 and dynamic rupture modeling efforts. We also discuss how our dynamic rupture model is
110 consistent with theoretical predictions that suggest the Garlock fault was in a dynamically
111 unfavorable set of conditions to co-rupture with the mainshock. Our analysis illustrates that both
112 normal and shear stress changes were highest on the Garlock fault at the end of mainshock rupture,
113 and could have been responsible for the observed geodetic creep.

114 **Methodology**

115 *Kinematic Slip Inversion*

116 We use a joint slip-inversion model that is based on static GPS, teleseismic and local
117 strong-ground motion datasets (Ji et al., 2002). The M6.4 foreshock and the M7.1 mainshock are
118 modeled with two and one fault segments, respectively. Here, the mainshock hypocenter has been
119 relocated to a depth of 3 km by the arrival times of nearby strong motion and broadband seismic
120 stations. Fault plane geometries roughly follow the USGS surface mapping and seismicity (Fig. 2)
121 and the fault parameters and hypocenters of both earthquakes are summarized in Table 1. We note
122 that the M7.1 mainshock ruptured bilaterally with a majority of slip concentrated within the upper
123 10 km and a peak slip amplitude of 4.7 m located ~10 km NW of the hypocenter (Fig. 2). On the
124 other hand, peak slip resolved for the foreshock is lower (1.3 m) and occurred mostly on the NE-
125 SW striking fault plane (Supplemental Fig 2). We use the slip inversion result for the mainshock
126 fault plane as input to our Coulomb stress change modeling.

127 We also compare our slip inversion results to those from other studies of the Ridgecrest
128 mainshock slip. We utilize seismic and GPS datasets to constrain the slip which is similar to the
129 approach by Liu et al., (2019). In contrast, other studies make use of a combination of high-rate
130 GPS and Interferometric Synthetic Aperture Radar imagery (InSAR, Goldberg et al., 2019; Ross
131 et al., 2019) or both InSAR and optimal image-tracking data (Barnhart et al., 2019). The details of
132 slip distribution and the relative locations of maximum slip vary between different studies. The
133 maximum slip is mostly shallower than (Barnhart et al., 2019), to the northwest of (Liu et al.,
134 2019), or slightly deeper (Ross et al., 2019) than the hypocenter location used in their inversion.
135 The kinematic slip inversion we present resolves two primary slip patches (i.e., Fig. 2), which have
136 similar slip amplitudes (4.7 m and 2.5 m) and slip patch locations (northwest and southeast of
137 hypocenter) to the Barnhart et al., (2019) and Liu et al., (2019) inversion results. Overall, our slip
138 distribution is consistent with published models, characterized by bilateral rupture propagation and
139 a shallow (< 10 km) slip distribution.

140 *Static Model: Coulomb Stress-Change*

141 Static stress changes are the final changes in the normal and shear stresses on the fault in
142 response to slip after all seismic waves have propagated through. Such stress changes during the
143 foreshock and mainshock of the Ridgecrest sequence have triggered thousands of aftershocks
144 (Ross et al., 2019). Coseismic stress changes have also been known to trigger or to reduce creep
145 after the earthquake (e.g., Allen et al., 1972, Bodin et al., 1994, Lienkaemper et al., 1997). Barnhart
146 et al. (2019) observed that an increase in the Coulomb stress change from the Ridgecrest
147 earthquake was correlated with the surface deformation after the earthquake. Studies have also
148 suggested that the M6.4 foreshock and other large foreshocks promoted the rupture of the
149 mainshock (Barnhart et al., 2019; Goldberg et al., 2019).

150 To assess static stress changes, we calculate the Coulomb stress change (Lin and Stein
151 2004; Toda et al. 2005), denoted by ΔCFS , caused by the foreshock on the mainshock and separate
152 the contribution of stress change from each of the two foreshock fault planes. We also calculate
153 the ΔCFS due to mainshock slip on the Garlock fault. We represent the Garlock fault geometry as
154 a plane with a strike, dip and rake of 70, 90, and 0 degrees, respectively. The strike of the Garlock
155 fault varies from 68° in the east to 84° in the west (Fig. 6), but we use 70° for the receiver fault as
156 it is closest to the strike of the western Garlock fault segment where the cluster of aftershocks
157 occurred. We use a friction coefficient of 0.6 and a depth of 5 km in both cases. To address
158 uncertainty in static friction level and hypocenter depth, we also examine how varying these
159 parameters influences our results. We compare the results from friction coefficients of 0.2, 0.4 and
160 0.6, and at 5 km depth, where peak slip occurred, and at 10 km depth, where the asperity with most
161 slip extends.

162 *Dynamic Model: Initial Conditions and Constraints*

163 We model the mainshock fault plane as a 100-km, planar 2-D crack embedded in a
164 homogeneous, isotropic, and linearly elastic medium with a shear-wave speed of 3.2 km/s. The
165 model domain is composed of rectangular quadrilateral elements enclosed on all sides by
166 absorbing boundaries (Supplementary Fig. S1). We choose a finite element size of 600-m with
167 four Gauss-Lobatto-Legendre nodes (NGLL) to resolve dynamic rupture propagation at seismic
168 frequencies up to 1 Hz for consistency with that resolved by the strong-motion dataset.

169 We select the linear slip-weakening friction law to control fault slip evolution and utilize
170 the 2-D spectral element code SEM2DPACK to solve for dynamic rupture propagation (Ampuero,

171 2009, <https://sourceforge.net/projects/sem2d/>). The critical-slip distance (D_c) is 0.3 m, which is
172 constant along the fault (except for ~ 15 km around the nucleation region) and is within the
173 plausible range of previous slip-weakening dynamic rupture simulations for other crustal
174 earthquakes of comparable magnitude and rupture dimension (e.g., Ma and Archuleta, 2006; Tinti
175 et al., 2009). If dynamic friction (μ_d) is below the static friction (μ_s) level, then the fault
176 experiences a strength-drop during coseismic rupture and its frictional behavior is slip-weakening;
177 conversely, if the dynamic friction is greater than static friction, there is no work available to grow
178 the propagating shear crack and the frictional behavior is slip-strengthening. The static friction
179 coefficient is everywhere 0.5 along the fault. The fault is slip-weakening ($\mu_d = 0.1$) along the
180 central 70 km segment (35 km southeast and northwest of hypocenter) and slip-strengthening ($\mu_d =$
181 0.7) everywhere else in order to prohibit rupture from breaking the entire fault.

182 Given that we represent a strike-slip fault as a Mode II in-plane crack, our stress and friction
183 conditions are relative to a region on the mainshock fault plane at depth. Our model aims to
184 reproduce the rupture propagation along the section of the fault that crosses through the main slip
185 asperity imaged in the kinematic inversion (Fig. 6). Effective normal stress is set to a constant
186 level of 50 MPa that is consistent with elevated pore-pressure levels in the middle of permeable
187 fault zones (Rice, 1992).

188 The initial shear stress distribution is a critical ingredient for any dynamic earthquake
189 rupture model and determines the dynamic stress drop which in turn governs slip amplitude. We
190 first calculate the static stress drop due to fault slip given by the kinematic inversion using a
191 computationally efficient algorithm (Fig. 3; Ripperger and Mai, 2004). Earthquakes can exhibit
192 total or near-total stress-drop due to strong dynamic weakening (e.g., Noda and Lapusta, 2013;
193 Brodsky et al., 2020), meaning that the final shear stress on the fault after an earthquake is at or
194 very near its dynamic fault strength level (the product of effective normal stress and dynamic
195 friction). We make this assumption to calculate our initial shear stress by adding the static stress
196 drop to the dynamic fault strength (Fig. 6).

197 Rupture is artificially nucleated in the middle of the fault using the time-weakening method
198 (Andrews, 1985). This technique requires twice the critical half-crack length ($2L_c$), an effective
199 friction level (μ_o), and a weakening time scale (T_c) after which the prescribed nucleation is turned
200 off and rupture spontaneously evolves according to the non-linear interaction between fault

201 strengths and stresses. Given the friction law parameters we assume for Mode II rupture in an
 202 elastic domain, $2L_c$ is given by

$$203 \quad 2L_c = \frac{2}{1-\nu} \frac{G}{\pi} \frac{\tau_s - \tau_d}{(\tau_o - \tau_d)^2} D_c \quad (1)$$

204 where G is the shear modulus (30 GPa), ν is Poisson's ratio, τ_s is the static fault strength,
 205 τ_d is the dynamic fault strength, τ_o is the initial shear stress, and μ_o is the effective friction
 206 coefficient calculated as the ratio between initial shear and effective normal stress amplitudes at
 207 the hypocenter. We determined that $2L_c$ of 2 km, μ_o of ~ 0.1 , and T_c of 10 seconds are necessary
 208 to nucleate and sustain spontaneous rupture.

209 **Results**

210 *Static Stress Change*

211 We find the foreshock increased the ΔCFS near the edges of the foreshock faults, especially
 212 at the intersection of Plane 2 and mainshock fault, but our relocated mainshock hypocenter is
 213 located in a region of slightly decreased ΔCFS (Fig. 4a; Supplemental Fig. S3). However, this
 214 result depends on the method used to locate the mainshock hypocenter and its uncertainty. For
 215 example, the ANSS hypocenter is closer to ours but at twice the depth, while the hypocenter
 216 resolved by Ross et al. (2019) is much closer to the foreshock hypocenter but at twice the depth as
 217 well. The hypocenters estimated by the ANSS catalog and by Ross et al. (2019) are located near
 218 the edges of different regions of positive ΔCFS . We also calculated the ΔCFS from both foreshock
 219 planes separately (Fig. 4b, c). We denote the foreshock fault parallel to the main fault as Plane 1
 220 and the NE-SW striking cross-fault as Plane 2. Plane 2 has a much larger slip compared to Plane
 221 1, with almost twice the peak slip. However, Plane 1 causes larger Coulomb stress change on the
 222 mainshock fault compared to Plane 2, as Plane 1 is closer.

223 We further calculate the ΔCFS on the Garlock fault due to mainshock slip and assess the
 224 effect of various friction coefficients and depths on our results. Overall, we find that the friction
 225 coefficient has a relatively small (i.e., a difference within ~ 0.1 MPa) impact on our ΔCFS results
 226 (Fig. 5). Larger friction coefficients increase the ΔCFS amplitude and changes its distribution
 227 slightly (Fig. 5). This is similar to Barnhart et al. (2019), where they found that their results are
 228 consistent for all friction coefficients that they tested. Changing the depth from 5 km to 10 km
 229 increases the ΔCFS amplitude and decreases the extent of the region of positive ΔCFS on the
 230 Garlock fault sharply. The amplitude difference is because the largest portion of mainshock slip
 231

232 extends to about 10 km depth, and the change in slip at this depth produces a larger ΔCFS than at
233 5 km depth. The region of positive ΔCFS in proximity to the creeping section of the Garlock fault
234 is most consistent in spatial extent with that of Barnhart et al. (2019) when we use a friction
235 coefficient of 0.2 and a depth of 5 km. Lastly, we find that the cluster of aftershocks on the Garlock
236 fault are unlikely to be simply explained by Coulomb static stress change from the mainshock as
237 the value of the stress change can be small and even negative (Fig. 5).

238 *Dynamic Earthquake Rupture model*

239 Our first goal is to explain the kinematic fault slip distribution using rupture dynamics. We
240 seek to reproduce the two primary patches of 2.5 m and 4.7 m slip southeast and northwest of the
241 hypocenter, respectively, (Fig. 3; 7a). We show the rupture history until 35 seconds to highlight
242 the arrest of both the northwest and southeast rupture fronts (Fig. 7).

243 The initial conditions and friction parameters outlined in the methods section gives a good
244 agreement between the kinematically imaged and dynamically modeled slip distributions. The
245 exception is the region near the hypocenter, where the dynamic rupture model overpredicts the
246 kinematic slip amplitude by ~ 0.8 meters (Fig. 7a). This is most likely due to our time-weakening
247 nucleation procedure, but is probably within the uncertainty of the true fault slip resolved by the
248 kinematic inversion. The distribution in dynamic stress drop is positive where higher slip is
249 concentrated, and negative in a small region southeast of the hypocenter and where we impose
250 slip-strengthening frictional behavior at the ends of the fault (Fig. 7b).

251 The bilateral mainshock dynamic rupture is overall heterogeneous and spatiotemporally
252 complex (Fig. 7c). There are three major asperities (i.e., relatively high dynamic stress-drop
253 regions) that contribute to several rupture-front accelerations (Fig. 7b, c). The model shows a slow
254 (< 1 km/s) rupture front propagating to the southeast for the first 5 seconds after nucleation ceases;
255 this southeast rupture front then accelerates to ~ 1.3 km/s before decelerating and arresting at 28
256 seconds (Figure 7c). In contrast, the northwest rupture front propagates at a more uniform speed
257 (~ 2.1 km/s) before decelerating and stopping at ~ 25 seconds. These rupture speeds are consistent
258 with recent kinematic models that prescribe a constant sub-Rayleigh mainshock rupture speed
259 (Goldberg et al., 2019; Liu et al., 2019; Ross et al., 2019). Rupture speed depends on how much
260 total elastic work is partitioned into radiated or fracture energy during the faulting process. Slower
261 ruptures (as observed during the Ridgecrest sequence) may be due to a relatively high fracture
262 energy consumed on the fault, consistent with the hypothesis that the Llfz is less compliant and

263 more energy was needed to break multiple fault segments (Goldberg et al., 2019; Liu et al., 2019;
264 Perrin et al., 2016). Our dynamic model shows that the mainshock rupture fronts do not exhibit
265 slip-rate amplitudes above 4 m/s and propagate at well below the Rayleigh wave speed.

266 *Temporal Stress Changes on the Garlock fault*

267 Using our dynamic rupture model, we investigate the stress contributions to a section of
268 the central Garlock fault during and after the Ridgecrest mainshock. Note that given the
269 limitation of our modeling domain, we cannot assess far-field dynamic stress contributions from
270 surface-wave amplitude changes. We instead focus on how the initial peak stresses carried by
271 near-field seismic waves impacted the Garlock fault during coseismic rupture.

272 The 2-D stress tensor in our model is for an isotropic body and yields three unique
273 components: σ_{xx} , σ_{yy} , and σ_{xy} . Only one component of the normal stress (σ_{yy}) and the shear stress
274 (σ_{xy}) are important to be considered further in our analysis. If we place the strike of the mainshock
275 fault plane on an east-west coordinate system, the angle between the mainshock and Garlock fault
276 planes (measured clockwise) is approximately 110 degrees (Fig. 1a). We therefore applied a
277 rotation of the stress field at a particular instant in time to represent the stress perturbation the
278 mainshock imparts to the Garlock fault (Fig. 8; see Supplemental Information). When this rotation
279 is performed at the final time-step, the rotated stress field is equivalent to the static stress change
280 on the Garlock fault. We observe an abrupt transition from negative to positive normal static stress
281 change as one crosses the intersection of the strike of the mainshock fault plane (Fig. 8a). The
282 shear stress change is slightly more complex with an asymmetric stress amplitude distribution
283 across the fault, but shows a very pronounced region of positive stress change that generally
284 coincides with the ~25-km long section of the central Garlock fault that underwent creep (Fig. 8b;
285 Barnhart et al., 2019; Xu et al., 2019). To confirm our static stress change analysis from the
286 dynamic model, we compare it to our ΔCFS calculation and find that its orientation and amplitude
287 are consistent (Supplemental Fig. S4).

288 We also calculate the temporal stress change on the central Garlock fault segment during
289 the Ridgecrest mainshock. We select one point near the creeping region on the Garlock fault (-60
290 km, -10 km; Fig. 9, 10) to show how normal and shear stresses change during mainshock rupture.
291 While propagation spontaneously arrests at near ~28 seconds towards the southeast, we simulate
292 rupture until 100 seconds to make sure stress changes relax to constant levels, which are attained
293 at 60 seconds (Fig. 11). This section of the central Garlock fault begins to experience a positive

294 normal stress change near 17.5 seconds (Fig. 9). During the main portion of coseismic rupture,
295 normal stress changes reach their maximum of ~ 0.3 MPa at 32 seconds (Fig. 9f, 11a). In contrast,
296 positive shear stress changes arrive at the Garlock fault in three distinct pulses (e.g., Fig. 10f, 11a).
297 Two of these positive shear stress change pulses arrive after the largest change in normal stress
298 change and continue to be above the normal stress change amplitude for the remainder of our
299 simulation (Fig. 10, 11a). The extrema of the normal and shear stress change amplitudes are
300 symmetric through time due to the alternating arrivals of compressional (P) and shear (SV) wave
301 motions.

302 **Discussion and Conclusion**

303 We show that stress changes during and after the Ridgecrest foreshocks and mainshock
304 may have influenced post-seismic creep on the central Garlock fault segment and brought certain
305 regions closer to coseismic failure. Our results also shed light on the temporal stress evolution on
306 the Garlock fault due to source dynamics. Because both normal and shear stresses vary during
307 coseismic rupture, evaluating their respective contribution is of critical importance to identifying
308 periods when stresses changes may have been favorable to engender the observed post-seismic
309 creep.

310 The Coulomb stress change results show that positive static stress changes were
311 experienced on the central Garlock fault due to mainshock slip (Fig. 4 and 5) and are coincident
312 with previously documented fault creep (Barnhart et al., 2019; Ross et al., 2019; Xu et al., 2020).
313 Among Coulomb stress changes calculated for different friction levels and depths, in only one case
314 (i.e., friction level of 0.6) is the positive static stress change seen to coincide with the section of
315 the Garlock fault that experienced a sizeable aftershock swarm (Fig. 5). This may indicate that
316 other post-seismic relaxation processes were at play to produce this aftershock pattern. When we
317 assess the ΔCFS through time we find that ΔCFS predominantly increases during mainshock
318 rupture and remains at a high level afterwards; this is evident from our dynamic model as the
319 normal stress change amplitude is mostly below the shear stress amplitude (Fig. 11b).

320 Temporal stress changes during the mainshock rupture also support predominantly positive
321 shear stress changes near this creeping Garlock region (Fig. 10), whereas positive and negative
322 normal stress distribution are observed on both sides of the projected intersection of the mainshock
323 and Garlock fault planes (Fig. 9). Our results for temporal normal and shear stress changes near
324 the Garlock fault agree with other dynamic rupture simulations that incorporate a complex 3-D

325 fault geometry (Lozos and Harris, 2019). Because positive normal stress changes serve to
326 strengthen the fault whereas positive shear stresses should bring the fault closer to failure, our
327 dynamic model offers one possible scenario that creep could have occurred as soon as ~15 seconds
328 after nucleation of the Ridgecrest mainshock when positive shear stresses began to arrive at the
329 Garlock fault. However, this is speculative given that we do not have information on the absolute
330 stress state of the Garlock fault prior to the aftershock/mainshock sequence.

331 Our dynamic model suggests that the largest shear stress changes (0.3 – 0.4 MPa) arrived
332 before and after the largest normal stress changes, but they are comparable in amplitude (Fig. 9,
333 10, 11a). Given this maximum shear stress change amplitude, we estimate approximately 0.1
334 centimeters of slip may have been triggered near the creeping section of the Garlock fault at a
335 depth less than 1 km (Supplemental Fig. S5a). We also test a model where creep on the Garlock
336 fault was exceptionally shallow (< 300 m depth; Schleicher et al., 2019) but the distribution of
337 creep is more heterogeneous. We still obtain a similar amount of creep that is consistent with the
338 shear stress change amplitude (Supplemental Fig. S5b). These estimates are lower than the
339 maximum magnitude of resolved surface creep (i.e., ~3 cm) documented earlier by Barnhart et al.,
340 (2019) and Ross et al., (2019), however. We cannot rule out the possibility that the maximum
341 resolvable creep was driven by cumulative strain-rate changes not seen by satellite observations
342 since the smallest observation window is at least five to six days after the mainshock (Barnhart et
343 al., 2019). Regardless of how much triggered creep was, extensometer data imply that it did not
344 extend very deep into the crust (Bilham and Castillo, 2020).

345 The fact that the Garlock fault did not coseismically fail is also supported by theoretical
346 considerations to the prestress state, rupture speed and fault orientation between the mainshock
347 and Garlock fault planes if they are connected (Poliakov et al., 2002; Kame et al., 2003). For a low
348 angle of maximum horizontal shear stress (SH_max) with respect to the fault (< 45 degrees), this
349 prestress state encourages rupture to bifurcate towards the compressional side, whereas a higher
350 angle (> 45 degrees) predicts that the rupture along the extensional side is more favorable
351 (Poliakov et al., 2002). We use stress tensor orientations inverted by Yang and Hauksson (2013)
352 from earthquake focal mechanisms in central and southern California to determine SH_max. We
353 find that the orientation of SH_max with respect to the North near the Ridgecrest region is between
354 zero and five degrees east of North (Fig. 1a). Given that the mainshock fault plane is approximately
355 oriented 45 degrees west of North, the SH_max orientation with respect to the mainshock fault

356 plane is ~ 50 degrees. This implies that the regional stress state would inhibit rupture propagation
357 to the Garlock fault, since the Garlock fault is oriented along the extensional side (Fig. 1a). Our
358 dynamic rupture model predicts an average rupture to shear-wave speed ratio of 0.4, and such low
359 levels are not likely to encourage rupture propagation to the Garlock fault, either (Kame et al.,
360 2003).

361 One aspect we could continue to explore in greater detail is how a fully dynamic model
362 incorporating segmented foreshock and mainshock fault planes changes the details of the temporal
363 stress changes on the Garlock fault. Given that the Ridgecrest sequence produced multiple
364 orthogonal faulting with some ruptures breaking the surface while others not (Ross et al., 2019),
365 we would expect the temporal stress change to accordingly reflect this complexity.

366 How the M6.4 foreshock and M7.1 mainshock Ridgecrest sequences changed the local
367 stress field in Southern California is a crucial question to consider given the proximity of these
368 events to other active faults (e.g., Garlock and San Andreas). Through a unique combination of
369 kinematic, static, and dynamic modeling, we present a physically coherent picture of the stress
370 changes on the central Garlock fault during and after the coseismic rupture of the M7.1 event. We
371 find that positive stress changes near the creeping section of the Garlock fault are observed during
372 and after coseismic rupture. We also show that the greatest shear stress change was comparable to
373 the greatest normal stress change, but arrived earlier during dynamic rupture; this may have
374 promoted a section of the Garlock fault to creep even before the Ridgecrest mainshock finished
375 slipping. Our dynamic models physically explain the resolved slip amplitude through the
376 mainshock hypocenter and reproduce the low sub-Rayleigh rupture speeds previously suggested
377 by kinematic rupture models.

378 **Data and Resources**

379 Static stress calculations are conducted using the Coulomb 3 software available from the
380 USGS website, <https://earthquake.usgs.gov/research/software/coulomb/>. All codes used in
381 dynamic model post-processing and figure creation as well as model input and output files are
382 archived and freely accessible on UM Deep Blue ([https:// deepblue.lib.umich.edu/](https://deepblue.lib.umich.edu/)). Seismic
383 waveform data used in the kinematic inversion are available upon request to Dr. Shengji Wei
384 (shjwei@ntu.edu.sg). Some figures in this paper were generated with the Generic Mapping Tools
385 (GMT 5, Wessel et al., 2013) or used colormap schemes from Crameri (2018).

386

387 **Acknowledgements**

388 This study was supported by the University of Michigan. M. D. Ramos and Y. Huang
389 acknowledge the funding support by the National Science Foundation through grant award
390 1663769.

391
392 **References**

- 393 Allen, C. R., Wyss, M., Brune, J. N., Grantz, A., and Wallace, R. E. (1972). Displacements on the
394 Imperial, Superstition Hills, and San Andreas faults triggered by the Borrego Mountain
395 earthquake, in The Borrego Mountain Earthquake of April 9, 1968. *U.S. Geol. Sur. Profess.*
396 *Paper*, 787, 87-104.
- 397
- 398 Ampuero, J. P. (2009). SEM2DPACK: A spectral element method tool for 2D wave propagation
399 and earthquake source dynamics, User's Guide, version 2.3.6. Retrieved from
400 <http://www.sourceforge.net/projects/sem2d/>
- 401
- 402 Andrews, D. J. (1985). Dynamic plane-strain shear rupture with a slip-weakening friction law
403 calculated by a boundary integral method. *Bull. Seismo. Soc. Of Amer.*, 75(1), 1–21.
- 404
- 405 Astiz, Luciana, Allen, C. R. (1983). Seismicity of the Garlock fault, California. *Bull. of the Seismo.*
406 *Soc. of Amer.*, 73(6), 1721–1734. <https://doi.org/10.1017/CBO9781107415324.004>
- 407
- 408 Barnhart, W. D., Hayes, G. P., & Gold, R. D. (2019). The July 2019 Ridgecrest, California,
409 Earthquake Sequence: Kinematics of Slip and Stressing in Cross-Fault Ruptures. *Geophys.*
410 *Res. Lett.*, (July), 859–867. <https://doi.org/10.1029/2019GL084741>
- 411
- 412 Bilham, R., and B. Castillo (2020). The July 2019 Ridgecrest, California, Earthquake Sequence
413 Recorded by Creepmeters: Negligible Epicentral Afterslip and Prolonged Triggered Slip
414 at Teleseismic Distances, *Seismol. Res. Lett.* XX, 1–14, doi: 10.1785/0220190293.
- 415
- 416 Bodin, P. and Gomberg, J. (1994). Triggered Seismicity and Deformation between the Landers,
417 California, and Little Skull Mountain, Nevada, Earthquakes. *Bulletin of the Seismological*
418 *Society of America*, 84, 3, 835-843.
- 419
- 420 Brodsky, E. E., Mori, J. J., Anderson, L., Chester, F. M., Conin, M., Dunham, E. M., ... Yang, T.
421 (2020). The State of Stress on the Fault Before, During, and After a Major Earthquake.
422 *Annu. Rev. Earth Planet. Sci.*, 48(1), annurev-earth-053018-060507.
423 <https://doi.org/10.1146/annurev-earth-053018-060507>
- 424
- 425 Crameri, F. (2018). Scientific colourmaps. Zenodo. <http://doi.org/10.5281/zenodo.1243862>
- 426
- 427 Dawson, T. E., McGill, S. F., & Rockwell, T. K. (2003). Irregular recurrence of paleoearthquakes
428 along the central Garlock fault near El Paso Peaks, California. *Jour. of Geophys. Res: Solid*
429 *Earth*, 108(B7). <https://doi.org/10.1029/2001jb001744>

- 431 Goldberg, D. E., Melgar, D., Thomas, A., Sahakian, V. J., Xu, X., Geng, J., & Crowell, B. W.
432 (2019, October 24). Complex Rupture of an Immature Fault Zone: A Simultaneous
433 Kinematic Model of the 2019 Ridgecrest, CA Earthquakes.
434 <https://doi.org/10.31223/osf.io/s79bk>
435
- 436 Hill, M. L. and T W. Dibblee (1953). San Andreas, Garlock and Big Pine faults, California, *Bull.*
437 *Geol Soc Am*, 64, 443-458.
438
- 439 Ji, C., D.J. Wald, and D.V. Helmberger (2002). Source description of the 1999 Hector Mine,
440 California earthquake; Part I: Wavelet domain inversion theory and resolution analysis,
441 *Bull. Seism. Soc. Am.*, Vol 92, No. 4. pp. 1192-1207.
442
- 443 Kame, N., Rice, J. R., & Dmowska, R. (2003). Effects of prestress state and rupture velocity on
444 dynamic fault branching. *Jour. of Geophys. Res: Solid Earth*, 108(B5), 1–21.
445 <https://doi.org/10.1029/2002jb002189>
446
- 447 King, G. and J. Nabelek, (1985). The role of fault bends in the initiation and termination of
448 earthquake rupture. *Science*, 228, 984-987.
449
- 450 Lienkaemper, J. J., Galehouse, J. S., Simpson, R. W. (1997). Creep response of the Hayward fault
451 to stress changes caused by the Loma Prieta earthquake. *Science*, 276, 5321, 2014-2016.
452 DOI: 10.1126/science.276.5321.2014
453
- 454 Lin, J. and R.S. Stein (2004). Stress triggering in thrust and subduction earthquakes, and stress
455 interaction between the southern San Andreas and nearby thrust and strike-slip faults. *J. of*
456 *Geophys. Res.*, 109, B02303, doi:10.1029/2003JB002607.
457
- 458 Liu, C., Lay, T., Brodsky, E. E., Dascher-Cousineau, K., & Xiong, X. (2019). Coseismic Rupture
459 Process of the Large 2019 Ridgecrest Earthquakes From Joint Inversion of Geodetic and
460 Seismological Observations. *Geophys. Res. Lett.* <https://doi.org/10.1029/2019GL084949>
461
- 462 Lozos, J. and Harris, R. (2019). Preliminary Dynamic Rupture Simulations of the July 2019 M6.4
463 and M7.1 Ridgecrest, California Earthquakes, Abstract S42C-05 presented at 2019 Fall
464 Meeting, AGU, San Francisco, CA, 9-14 Dec., 2019.
465
- 466 Ma, S. and Archuleta, R.J., (2006). Radiated seismic energy based on dynamic rupture models of
467 faulting, *J. Geophys. Res.*, 111, doi:10.1029/2005JB004055.
468
- 469 Madugo, C. M., Dolan, J. F., & Hartleb, R. D. (2012). New paleoearthquake ages from the western
470 Garlock fault: Implications for regional earthquake occurrence in Southern California. *Bull.*
471 *of the Seismo. Soc. of Amer.*, 102(6), 2282–2299. <https://doi.org/10.1785/0120110310>
472
- 473 McGill, S. F., and K. Sieh (1991). Surficial offsets on the central and eastern Garlock fault
474 associated with prehistoric earthquakes, *J. Geophys. Res.*, 96, 21,597–21,621.
475

- 476 Noda, H., and N. Lapusta (2013). Stable creeping fault segments can become destructive as a result
477 of dynamic weakening, *Nature*, 493, 518–521, doi:10.1038/nature11703.
478
- 479 Perrin, C., Manighetti, I., Ampuero, J.-P., Cappa, F., & Gaudemer, Y. (2016). Location of largest
480 earthquake slip and fast rupture controlled by along-strike change in fault structural maturity
481 due to fault growth. *Jour. of Geophys. Res: Solid Earth*, 121(5), 3666–3685.
482 <https://doi.org/10.1002/2015JB012671>
483
- 484 Poliakov, A. N. B., Dmowska, R., & Rice, J. R. (2002). Dynamic shear rupture interactions with
485 fault bends and off-axis secondary faulting. *Jour. of Geophys. Res.*, 107(B11), ESE 6-1-
486 ESE 6-18. <https://doi.org/10.1029/2001jb000572>
487
- 488 Rice, J. R. (1992). Fault Stress States, Pore Pressure Distributions, and the Weakness of the San
489 Andreas Fault. *Inter. Geophys.*, 51(C), 475–503. [https://doi.org/10.1016/S0074-
490 6142\(08\)62835-1](https://doi.org/10.1016/S0074-6142(08)62835-1)
491
- 492 Ripperger, J., & Mai, P. M. (2004). Fast computation of static stress changes on 2D faults from
493 final slip distributions. *Geophys. Res. Lett.*, 31(18), 2–5.
494 <https://doi.org/10.1029/2004GL020594>
495
- 496 Ross, Z. E., Idini, B., Jia, Z., Stephenson, O. L., Zhong, M., Wang, X., ... Moore, A. W. (2019).
497 2019 Ridgecrest earthquake sequence. *Science*, 3665(October), 346–351.
498
- 499 Schleicher, L. S., Huang, M., Allison, K. L., and Anderson, R. J. (2019). Seismic hazard
500 implications of post-seismic deformation and stress transfer from the 2019 Searles Valley
501 California Earthquakes, Abstract S41C-08 presented at 2019 Fall Meeting, AGU, San
502 Francisco, CA, 9-14 Dec., 2019.
503
- 504 Toda, S., R. S. Stein, K. Richards-Dinger and S. Bozkurt (2005). Forecasting the evolution of
505 seismicity in southern California: Animations built on earthquake stress transfer. *J.*
506 *Geophys. Res.*, 110, B05S16, doi:10.1029/2004JB003415.
507
- 508 Tinti, E., Cocco, M., Fukuyama, E., & Piatanesi, A. (2009). Dependence of slip weakening
509 distance (D_c) on final slip during dynamic rupture of earthquakes. *Geophys. Jour. Int.*,
510 177(3), 1205–1220. <https://doi.org/10.1111/j.1365-246X.2009.04143.x>
511
- 512 Wessel, P., W. H. F. Smith, R. Scharroo, J. F. Luis, and F. Wobbe, Generic Mapping Tools:
513 Improved version released, *EOS Trans. AGU*, 94, 409-410, 2013.
514
- 515 Xu, X., D. T. Sandwell, and B. Smith-Konter (2020). Coseismic Displacements and Surface
516 Fractures from Sentinel-1 InSAR: 2019 Ridgecrest Earthquakes, *Seismol. Res. Lett.* XX,1–
517 7, doi: 10.1785/0220190275.
518
- 519 Yang, W. and Hauksson, E., (2013). The tectonic crustal stress field and style of faulting along the
520 Pacific North America Plate boundary in Southern California, *Geophys. Jour. Int.*, 194, 100-
521 117, doi: 10.1093/gji/ggt113

522 **Author Mailing Addresses**

- 523 1. Marlon D. Ramos, Jing Ci Neo, Prithvi Thakur, Yihe Huang
524 2. Shengji Wei

525

526 Authors one through four may be contacted at:

527

528 Department of Earth and Environmental Sciences

529 University of Michigan

530 Room 2534

531 Attn: Marlon D. Ramos, Jing Ci Neo, Prithvi Thakur, Yihe Huang

532 1100 North University Avenue

533 Ann Arbor, MI 48109-1005

534 Author five may be contacted at:

535 Earth Observatory of Singapore

536 Nanyang Technological University

537 Attn: Wei Shengji

538 N2-01A-08

539 50 Nanyang Ave, Singapore 639798

540

541

542

543

544

545

546

547

548

549

550

551

552 **List of Tables**

553
554
555
556
557
558
559

Table 1

Coulomb stress-change parameters of the mainshock and aftershock fault planes. Hypocenter location (latitude, longitude, depth) and maximum slip amplitude (meters) from kinematic inversion are also listed.

	M_w	Hypocenter	Strike	Dip	Rake	Peak Slip (m)
Mainshock	7.1	35.772N -117.602E 3 km	322	81	-170	4.7
Foreshock	6.4	35.705N -117.506E 9 km	318 228	88 81	-172 0	1.3 0.74

560
561
562
563
564
565
566
567
568
569
570
571
572
573
574
575
576
577
578
579
580

581 **List of Figure Captions**

582

583 **Figure 1.** 2019 Ridgecrest Sequence. A) Dynamic rupture model framework in a compressive
584 stress field. The mainshock is modeled as a mode II shear-crack that is ~ 110 degrees (clockwise)
585 from the Garlock fault. Whether rupture will branch from the mainshock to Garlock fault is
586 determined by the rupture speed (v_r), prestress level on the fault, and maximum compressional
587 stress direction (SH_max). B) Study area with foreshock-mainshock focal mechanism solutions
588 (USGS) and the western, central, and eastern Garlock fault segments. Yellow box denotes
589 approximate location of geodetically imaged fault creep. SH_max field from Yang and Hauksson
590 (2013). SAF = San Andreas Fault.

591

592 **Figure 2.** Ridgecrest slip inversion results obtained using teleseismic and local strong-motion data.
593 The mainshock fault is 100 km long, with foreshock fault plane 1 and foreshock plane 2 indicated.
594 The black line denotes the surface trace of the Garlock fault.

595

596 **Figure 3.** Mainshock slip inversion results.

597

598 **Figure 4.** Coulomb stress change due to foreshock plane 1 and 2 on the mainshock fault plane
599 calculated at a depth of 5 km and with a friction coefficient of 0.6. A) The combined effect of slip
600 on the mainshock and both aftershock fault planes. B) The Coulomb stress change from plane 1
601 which is parallel to the main fault plane. C) Coulomb stress change from plane 2, which is the NE-
602 SW striking cross-fault. The aftershocks depicted are the earthquakes that occurred after the
603 foreshock and do not include those induced from mainshock stress changes.

604

605 **Figure 5.** Coulomb stress change of the mainshock on a receiver fault of 70° strike and 90° dip,
606 approximating the leftmost part of the Garlock fault in this figure. Top: Coulomb stress-change
607 results for a 5 km depth source at friction coefficients of 0.2, 0.4, and 0.6. Bottom: Coulomb stress-
608 change results for a 10 km depth source with the same friction coefficients.

609

610 **Figure 6.** Static stress-drop (top) and initial shear stress (bottom) along the mainshock fault
611 plane. Static stress-drop is calculated assuming a homogeneous, Poisson medium and initial
612 shear stress is computed using the complete stress-drop assumption. We select an initial shear
613 stress profile through the main asperity at 3 km depth (dashed black line) as a starting condition
614 for our 2-D dynamic rupture models.

615

616 **Figure 7.** A) Along-fault slip distribution resolved by the kinematic slip inversion (black line)
617 and that calculated from the dynamic rupture model (dashed blue line). The earthquake is nucleated
618 at (0,0) as indicated by the magenta star. B) Dynamic stress-drop along the fault. Location shown
619 in Figure 6. C) Spatiotemporal and bilateral rupture history predicted by the dynamic rupture
620 model. Colorbar denotes slip-rate and the slope of the gradient between zero and peak slip-rate
621 signifies the rupture front speed (solid white lines). Both rupture fronts propagate at sub-Rayleigh
622 wave speed.

623

624

625 **Figure 8.** Static stress-change field in the modeling domain rotated to the strike of the Garlock
626 fault. A) normal stress and B) shear stress. Garlock fault trace (dashed black line) and Ridgecrest
627 mainshock fault (bold black line) are superimposed onto the figure. Yellow box denotes
628 approximate location of the creeping region (Barnhart et al., 2019).

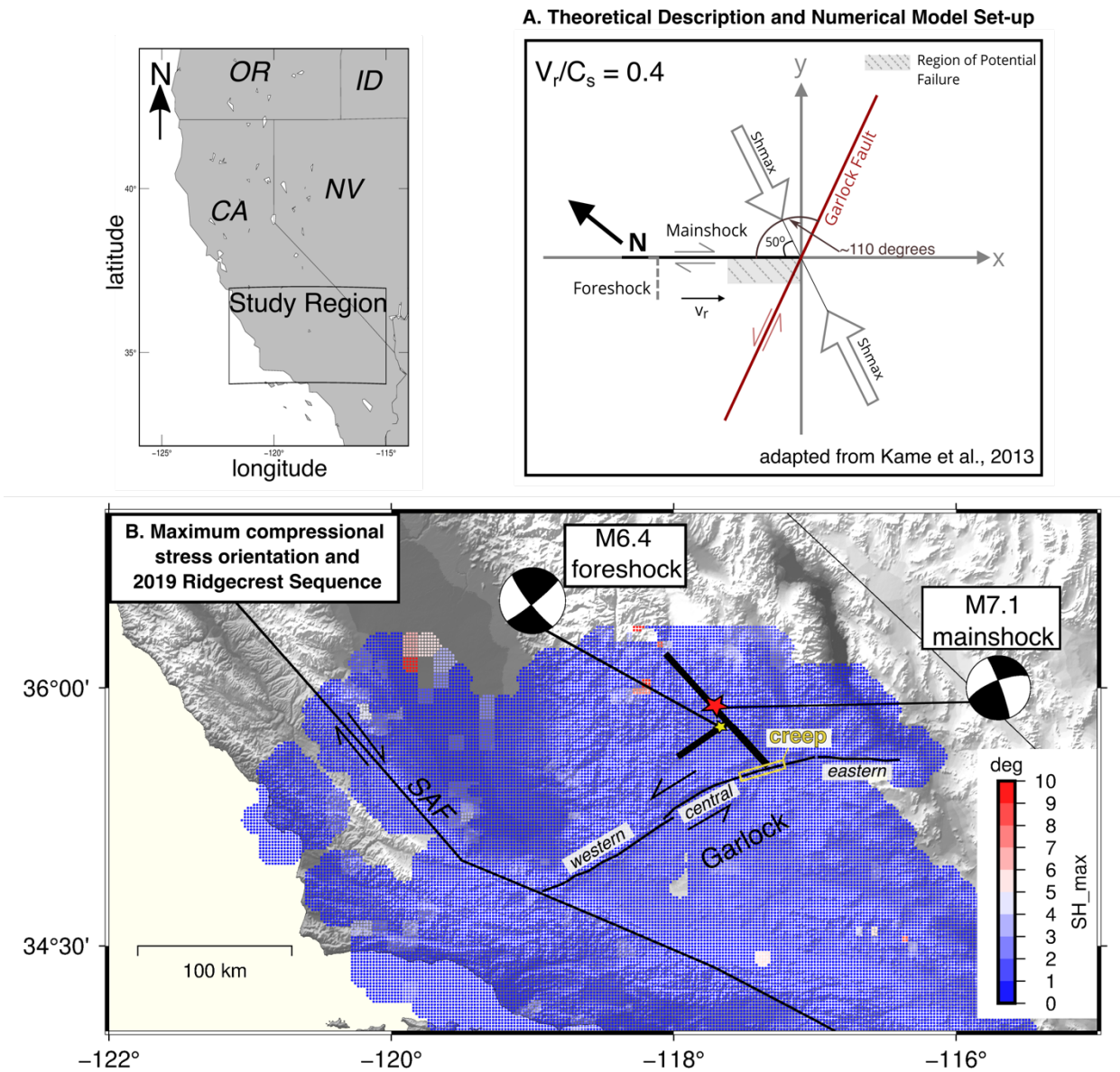
629
630 **Figure 9.** Normal stress changes (σ_{yy}) at various moments in time on the central Garlock fault
631 during coseismic rupture of the mainshock. A point on the Garlock (-10km, -60 km) is selected
632 to visualize the stress amplitude variability (yellow dot). Subfigures A through E represent σ_{yy}
633 from 17.5 to 50 during rupture propagation. Subfigure F shows the time-history of σ_{yy} where the
634 blue squares denote the amplitude change at each of the normal stress snapshots (A-E). GF =
635 Garlock fault.

636
637 **Figure 10.** Similar to Fig. 9, but shear stress changes (σ_{xy}) during coseismic rupture. σ_{xy} exhibits
638 three distinct peaks in its temporal stress-change on the Garlock fault at ~28, 38, and 50 seconds.

639
640 **Figure 11.** Stress change evolution on a section of the Garlock fault during the entire Ridgecrest
641 simulation. A) Normal and shear stress change. B) Coulomb stress change for various friction
642 coefficients assessed in the static stress change analysis. Note that we plot the temporal stress
643 change starting at 10 seconds because this is when the nucleation procedure ceases.

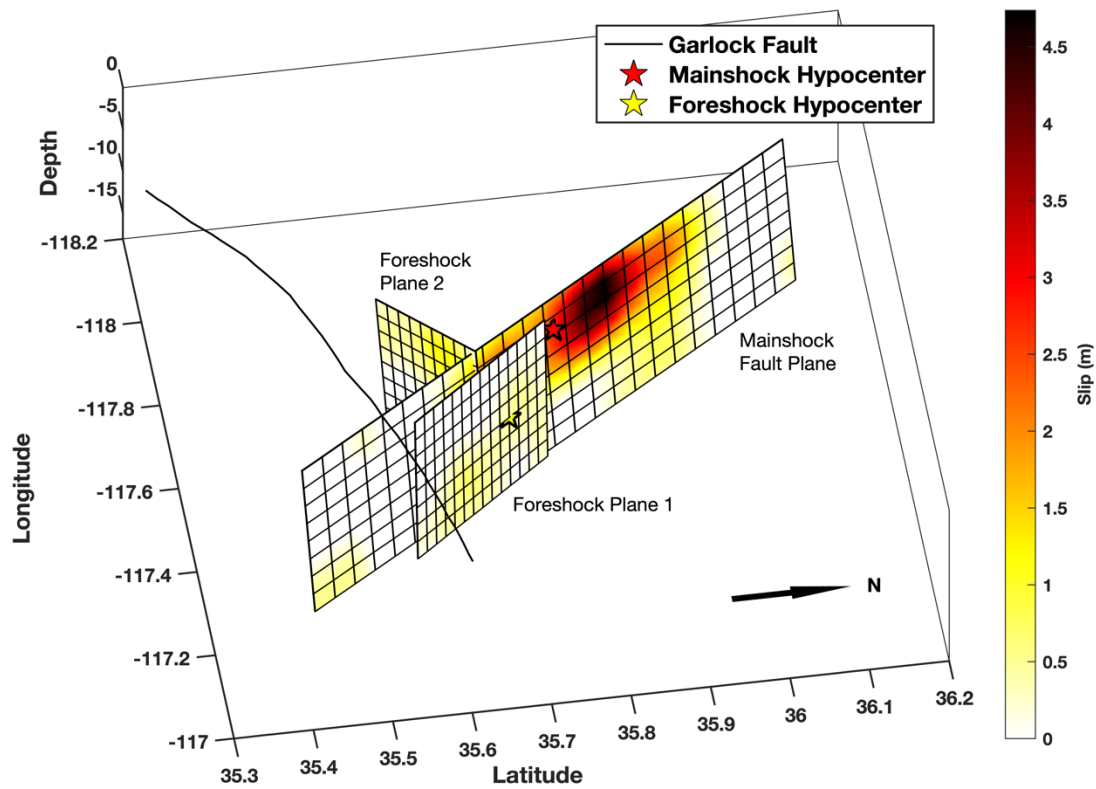
644
645
646
647
648
649
650
651
652
653
654
655
656
657
658
659
660
661
662
663
664
665
666
667
668
669
670

671 **Figures**
672

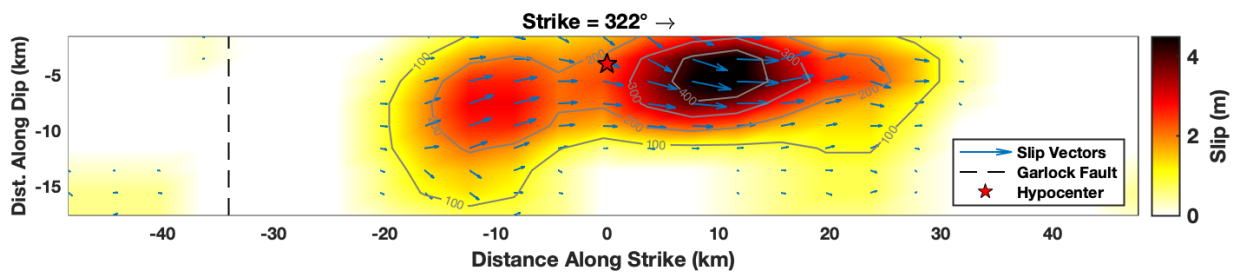


673 **Figure 1.** 2019 Ridgecrest Sequence. A) Dynamic rupture model framework in a compressive
674 stress field. The mainshock is modeled as a mode II shear-crack that is ~110 degrees (clockwise)
675 from the Garlock fault. Whether rupture will branch from the mainshock to Garlock fault is
676 determined by the rupture speed (v_r), prestress level on the fault, and maximum compressional
677 stress direction (SH_{max}). B) Study area with foreshock-mainshock focal mechanism solutions
678 (USGS) and the western, central, and eastern Garlock fault segments. Yellow box denotes
679 approximate location of geodetically imaged fault creep. SH_{max} field from Yang and Hauksson
680 (2013). SAF = San Andreas Fault.

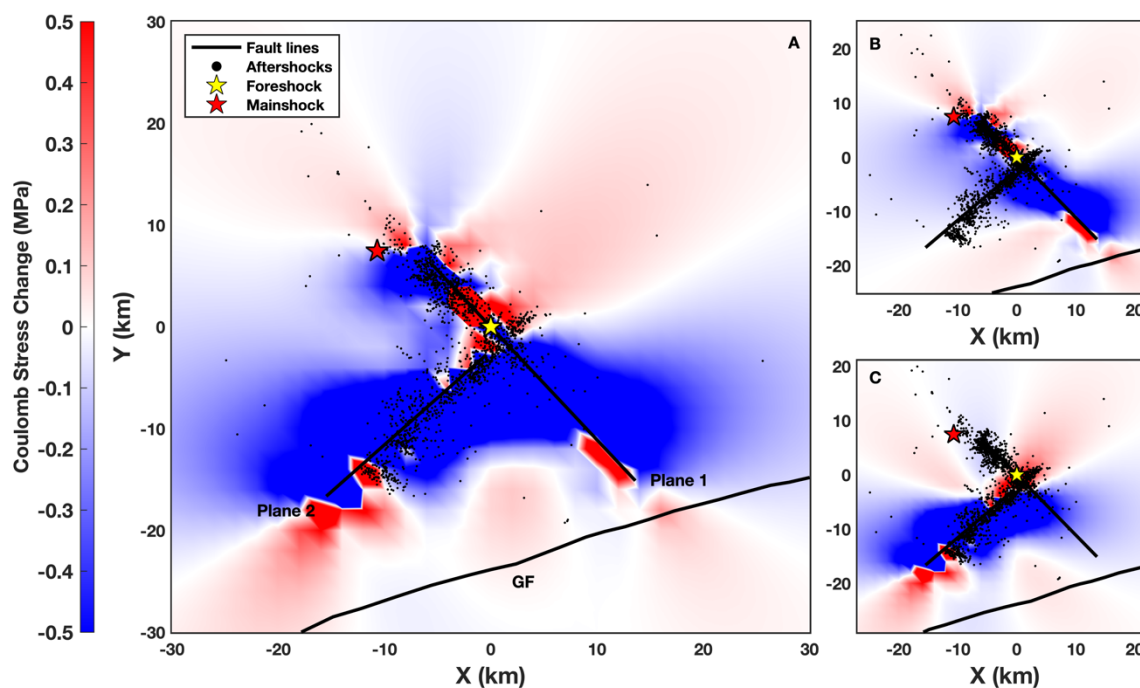
681
682
683
684
685



686
 687 **Figure 2.** Ridgecrest slip inversion results obtained using teleseismic and local strong-motion data.
 688 The mainshock fault is 100 km long, with foreshock fault plane 1 and foreshock plane 2 indicated.
 689 The black line denotes the surface trace of the Garlock fault.
 690
 691

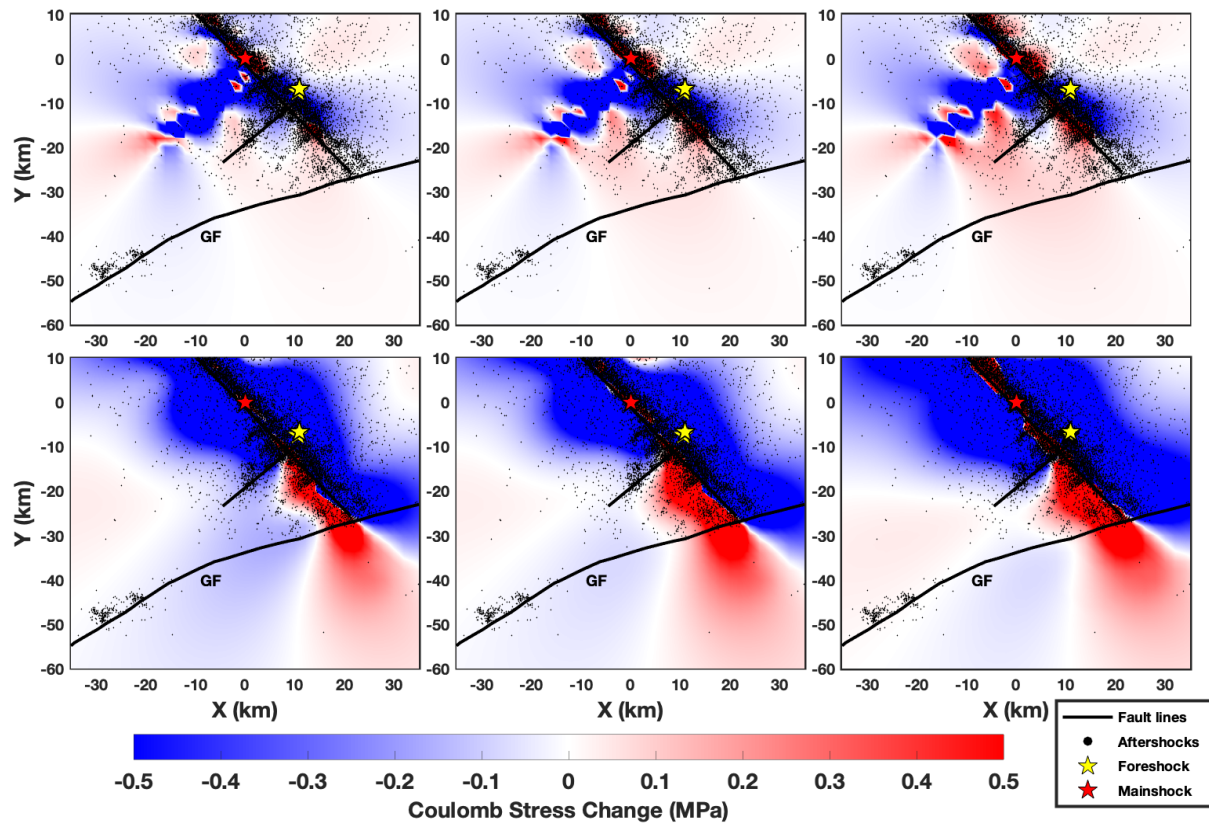


692
 693 **Figure 3.** Mainshock slip inversion results.
 694
 695
 696



697
 698 **Figure 4.** Coulomb stress change due to foreshock plane 1 and 2 on the mainshock fault plane
 699 calculated at a depth of 5 km and with a friction coefficient of 0.6. A) The combined effect of slip
 700 on the mainshock and both aftershock fault planes. B) The Coulomb stress change from plane 1
 701 which is parallel to the main fault plane. C) Coulomb stress change from plane 2, which is the NE-
 702 SW striking cross-fault. The aftershocks depicted are the earthquakes that occurred after the
 703 foreshock and do not include those induced from mainshock stress changes.

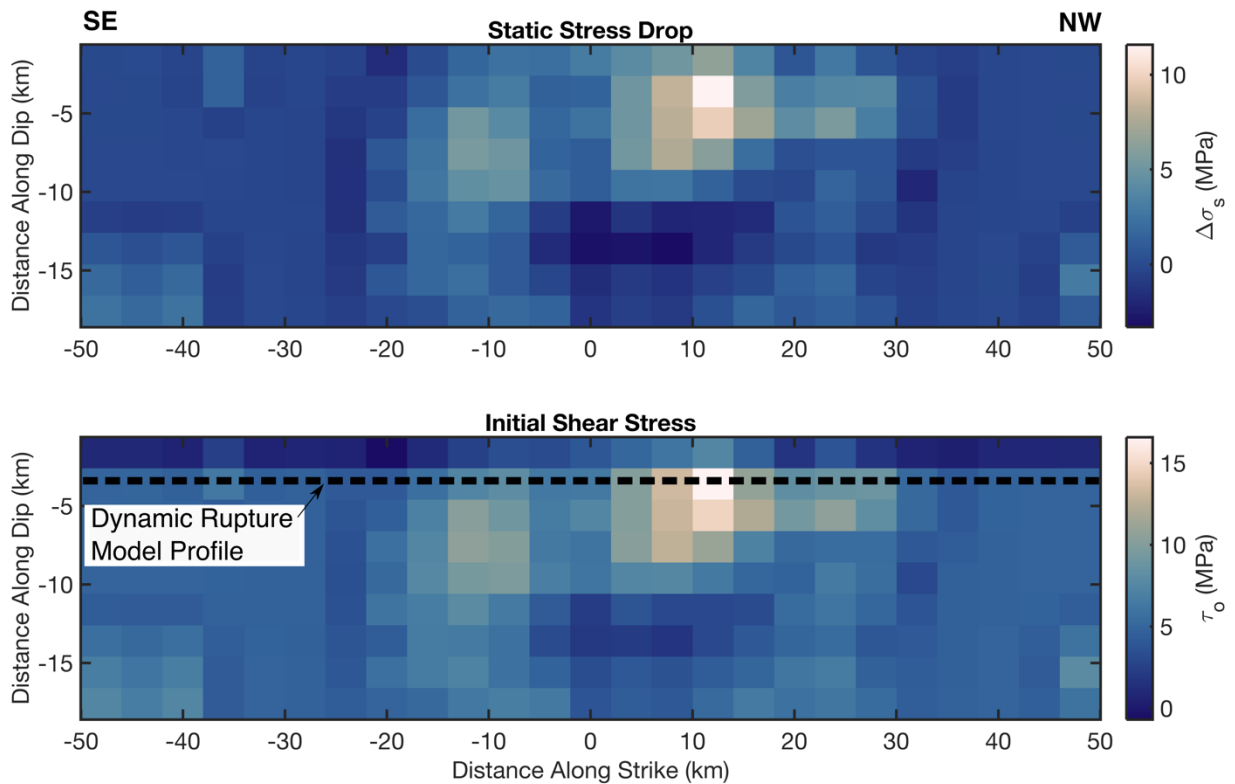
704
 705
 706



707
708
709
710
711
712
713
714
715
716
717
718
719
720
721
722
723
724
725
726
727
728
729
730
731

Figure 5. Coulomb stress change of the mainshock on a receiver fault of 70° strike and 90° dip, approximating the leftmost part of the Garlock fault in this figure. Top: Coulomb stress-change results for a 5 km depth source at friction coefficients of 0.2, 0.4, and 0.6. Bottom: Coulomb stress-change results for a 10 km depth source with the same friction coefficients.

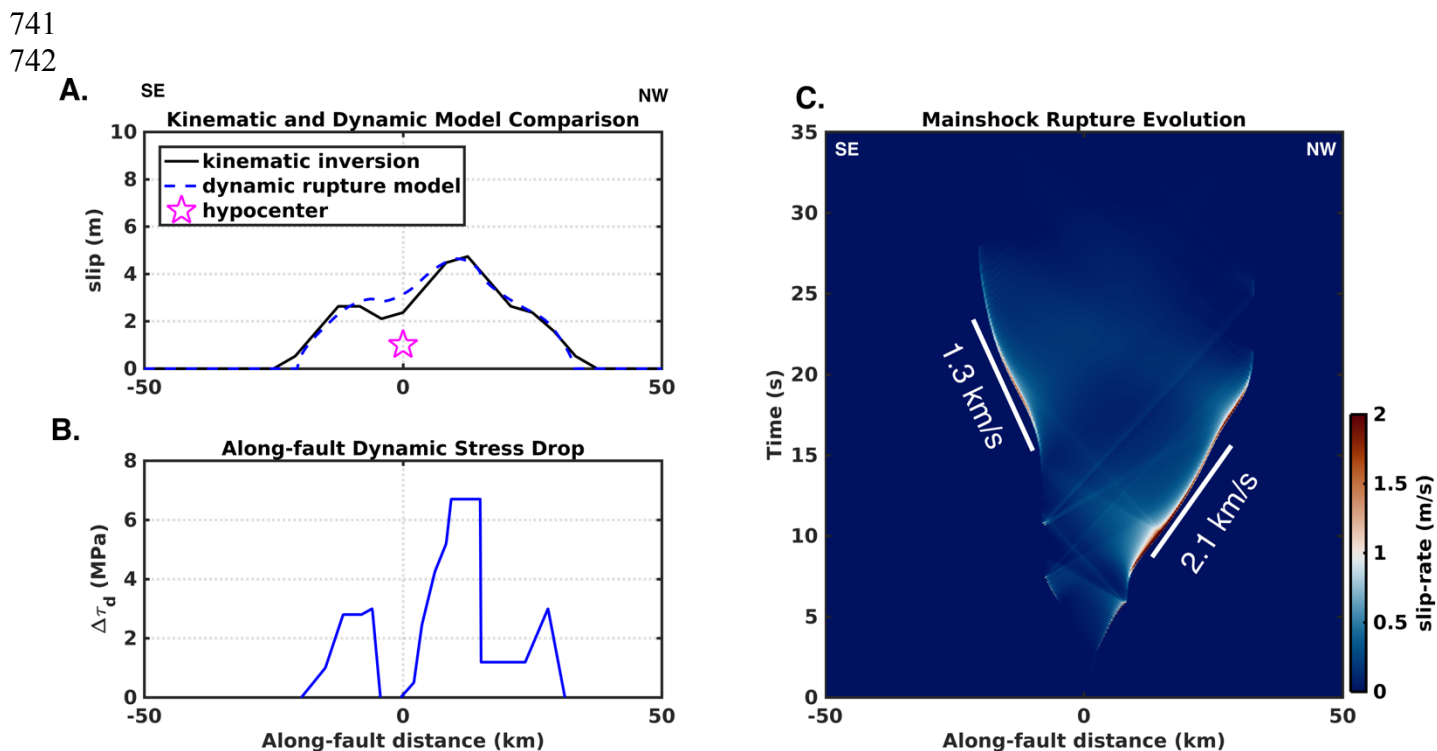
732



73: **Figure 6.** Static stress-drop (top) and initial shear stress (bottom) along the mainshock fault plane.
 734 Static stress-drop is calculated assuming a homogeneous, Poisson medium and initial shear stress
 735 is computed using the complete stress-drop assumption. We select an initial shear stress profile
 736 through the main asperity at 3 km depth (dashed black line) as a starting condition for our 2-D
 737 dynamic rupture models.
 738

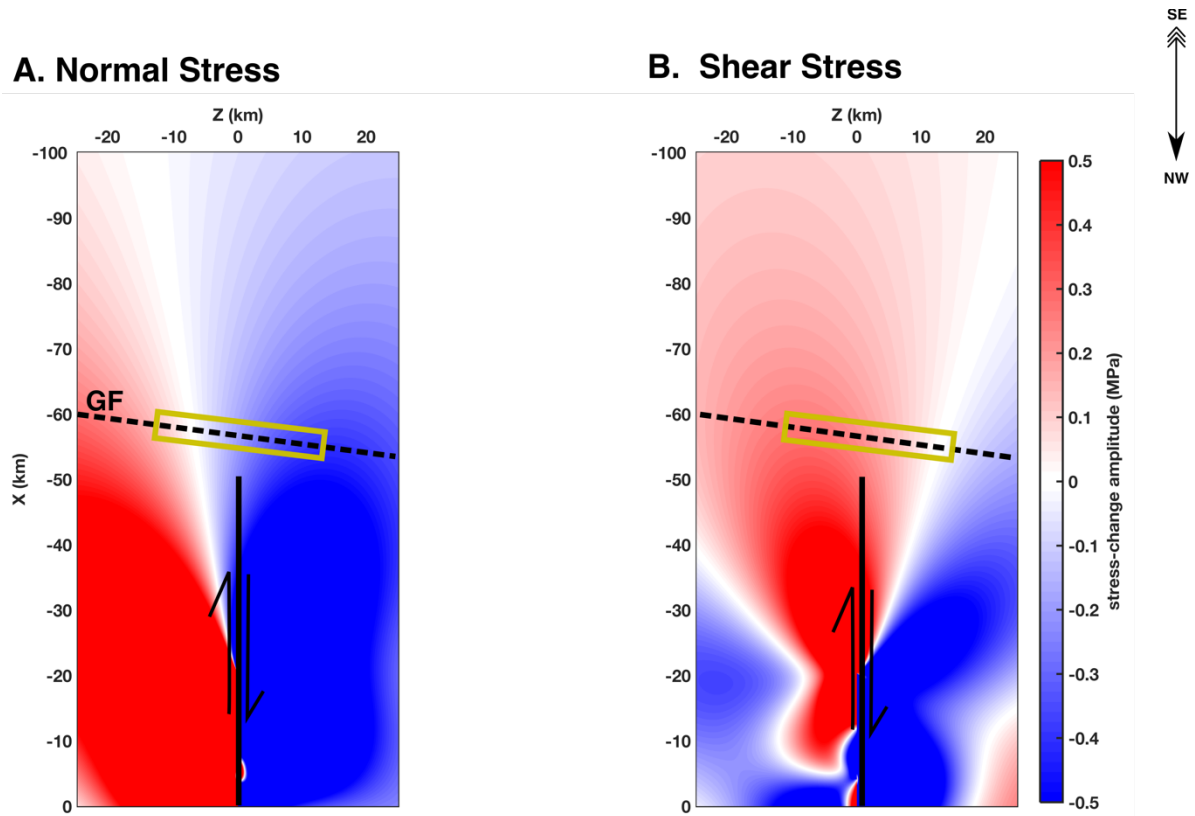
739

740



743
744 **Figure 7.** A) Along-fault slip distribution resolved by the kinematic slip inversion (black line)
745 and that calculated from the dynamic rupture model (dashed blue line). The earthquake is nucleated
746 at (0,0) as indicated by the magenta star. B) Dynamic stress-drop along the fault. Location shown
747 in Figure 6. C) Spatiotemporal and bilateral rupture history predicted by the dynamic rupture
748 model. Colorbar denotes slip-rate and the slope of the gradient between zero and peak slip-rate
749 signifies the rupture front speed (solid white lines). Both rupture fronts propagate at sub-Rayleigh
750 wave speed.

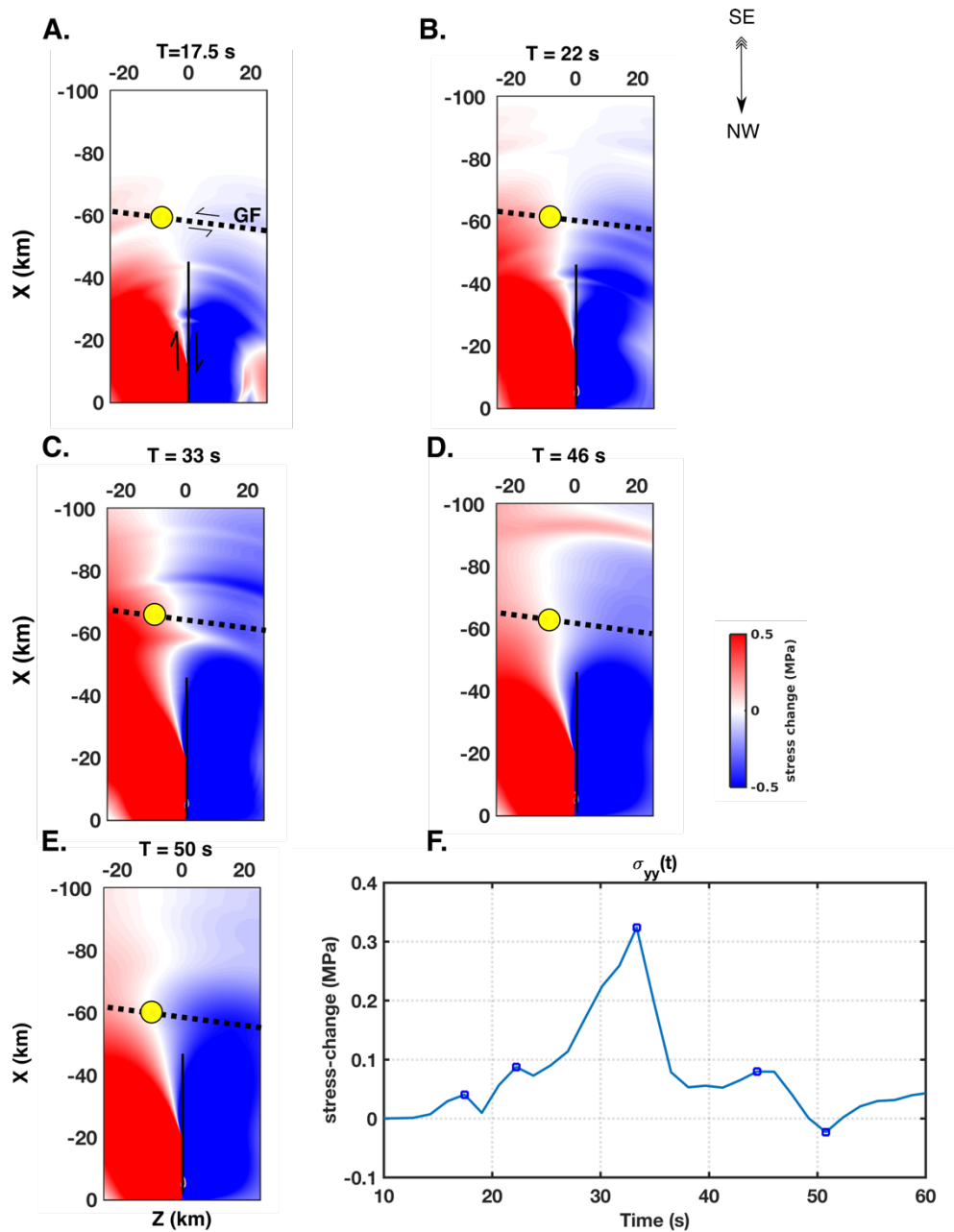
751
752
753
754
755



756
757
758
759
760
761
762
763
764
765
766
767
768
769
770
771
772
773
774
775
776
777
778
779
780

Figure 8. Static stress-change field in the modeling domain rotated to the strike of the Garlock fault. A) normal stress and B) shear stress. Garlock fault trace (dashed black line) and Ridgecrest mainshock fault (bold black line) are superimposed onto the figure. Yellow box denotes approximate location of the creeping region (Barnhart et al., 2019).

781



782

783

784

785

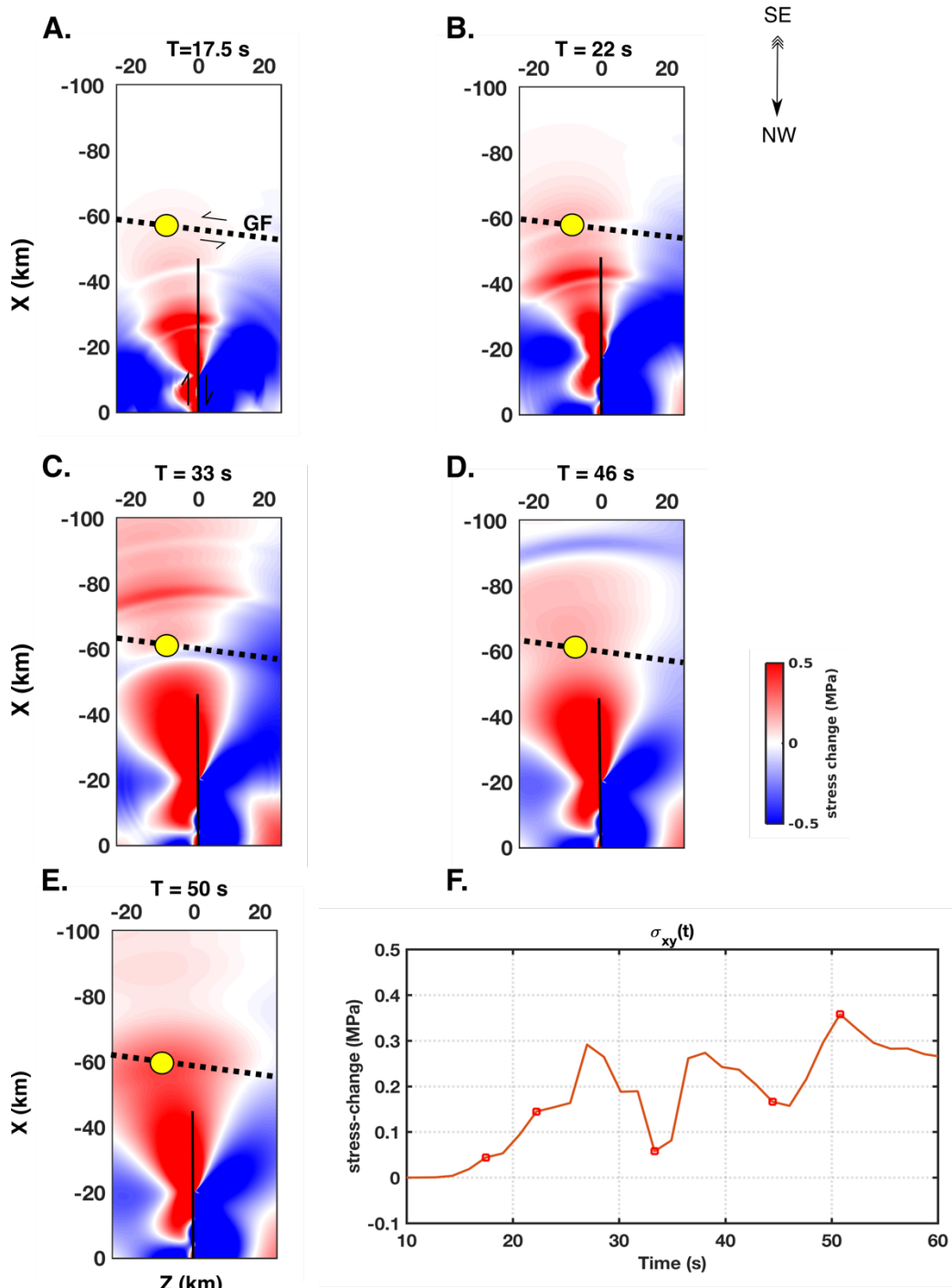
786

787

788

789

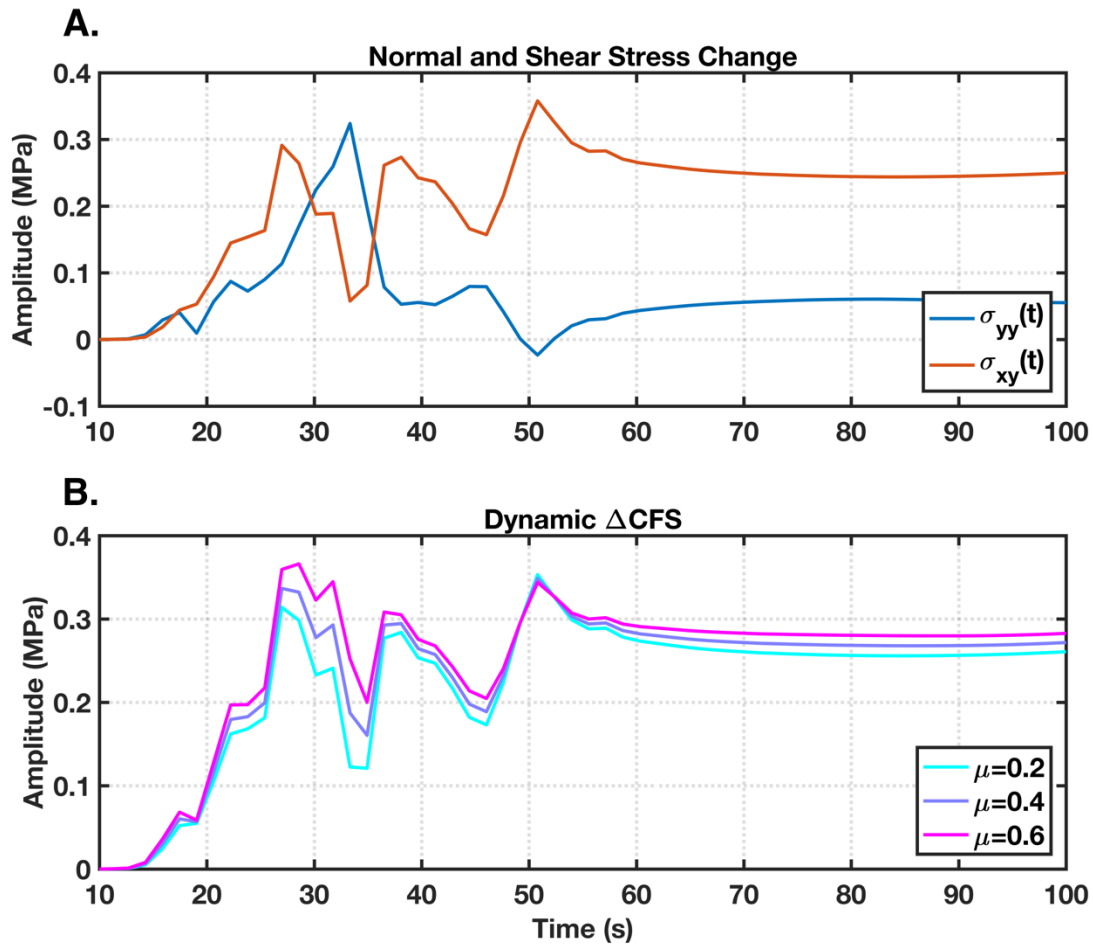
Figure 9. Normal stress changes (σ_{yy}) at various moments in time on the central Garlock fault during coseismic rupture of the mainshock. A point on the Garlock (-10km, -60 km) is selected to visualize the stress amplitude variability (yellow dot). Subfigures A through E represent σ_{yy} from 17.5 to 50 seconds during rupture propagation. Subfigure F shows the time-history of σ_{yy} where the blue squares denote the amplitude change at each of the normal stress snapshots (A-E).



790
791
792
793
794
795
796
797
798

Figure 10. Similar to Fig. 9, but shear stress changes (σ_{xy}) during coseismic rupture. σ_{xy} exhibits three distinct peaks in its temporal stress-change on the Garlock fault at ~28, 38, and 50 seconds.

799



800
 801 **Figure 11.** Stress change evolution on a section of the Garlock fault during the entire Ridgecrest
 802 simulation. A) Normal and shear stress change. B) Coulomb stress change for various friction
 803 coefficients assessed in the static stress change analysis. Note that we plot the temporal stress
 804 change starting at 10 seconds because this is when the nucleation procedure ceases.